Journal of Non-Newtonian Fluid Mechanics 348 (2026) 105544

Contents lists available at ScienceDirect

Journal of Non-Newtonian Fluid Mechanics

journal homepage: www.elsevier.com/locate/jnnfm

Full length article

Numerical simulations of the stretching and relaxation dynamics of viscoelastic freestanding liquid films

Davide Amoroso, Massimiliano M. Villone *

Department of Chemical, Materials, and Manufacturing Engineering, University of Naples Federico II, P.le Tecchio, 80, Naples, 80125, Italy

ARTICLE INFO

Keywords:
Freestanding liquid films
Viscoelasticity
Biaxial deformation
Leveling dynamics

ABSTRACT

Understanding the role of elasticity in the stretching and relaxation processes of freestanding liquid films is a key step in the study of two-phase systems such as foams and emulsions. This work employs numerical simulations based on the finite element method to investigate the dynamics of viscoelastic films undergoing biaxial extensional deformation followed by relaxation. Two constitutive equations (Oldroyd-B and Giesekus) are employed to capture the effects of elasticity, viscosity, and capillarity. A parametric study is performed to assess the effects of Weissenberg-number-variations on elastic energy accumulation and film thickness evolution. Distinct behaviors are found for the two rheological models: the relaxation of Oldroyd-B films is characterized by an increase in thickness at the center, referred to as 'elastic leveling'; in contrast, Giesekus films exhibit a decrease in thickness that we define 'elastic anti-leveling'. Our results highlight the critical role of viscoelastic effects in governing the transient behavior of freestanding films beyond classical capillary-driven flow.

1. Introduction

Freestanding liquid films are liquid layers simultaneously exposed on both sides to different surrounding fluids, which can be either gases or other liquids [1,2]. Representative examples are foams, emulsions, polymeric films, and membranes [3–7]. The scientific interest in freestanding liquid films is due to several factors. First, film stability is critical for foams and emulsions, because it directly affects the stability of the overall macroscopic structure. Second, the absence of a supporting substrate eliminates substrate-induced effects, allowing the ideal study of phenomena such as glass transition and confinement behavior in polymeric liquids. This also allows for the realization of effectively infinite slip-length boundaries [8,9]. Furthermore, when such films are perturbed, the relaxation dynamics toward equilibrium can provide insight into molecular-scale interfacial friction and glassy dynamics [10–12].

A study by Ilton et al. [13] investigated the relaxation behavior of a Newtonian polystyrene (PS) film with a stepped profile. In this context, the relaxation mechanism driven by surface tension and opposed by viscous forces is called 'capillary leveling flow'. By reconstructing the film thickness profiles using atomic force microscopy (AFM), the authors observed that the extent of the intermediate region, w, namely, the film region connecting the central part with lower thickness with the peripheral part with higher thickness, evolves over time, t, according to the scaling law $w \propto t^{1/2}$. This experimentally observed behavior is consistent with theoretical predictions derived from the Navier–Stokes equations under the long-wave (lubrication) approximation [14,15]. Notably, the scaling law differs from that characterizing supported films, reading $w \propto t^{1/4}$ [16,17]. A more recent study by Ferraro et al. [18] investigated the behavior of Newtonian polydimethylsiloxane (PDMS) deposited in the hole of a motorized iris diaphragm (MID). The opening of the MID induces a biaxial extensional deformation of the liquid, resulting in the formation of a freestanding film with a sigmoidal thickness profile. The authors analyzed the relaxation dynamics of the film, which was, again, governed by capillary leveling flow. The film thickness evolution was monitored quantitatively using digital holography. The results showed that, during the leveling process, the scaling law identified by Ilton and co-authors holds true. In addition, finite-element-method (FEM) simulations were performed, showing good agreement with the experimental data.

Although some studies have addressed the role of elasticity in freestanding films, particularly with respect to their stability [19,20], there remains the need to better understand how constitutive and operational parameters influence their deformation and relaxation dynamics. Indeed, in such systems, in addition to the interplay between surface tension, which drives the flow, and viscous resistance, which goes against it, elastic energy storage introduces an additional mechanism that can significantly affect the evolution of the film.

* Corresponding author.
E-mail address: massimilianomaria.villone@unina.it (M.M. Villone).

https://doi.org/10.1016/j.jnnfm.2025.105544
Received 5 August 2025; Received in revised form 4 December 2025; Accepted 9 December 2025
Available online 19 December 2025

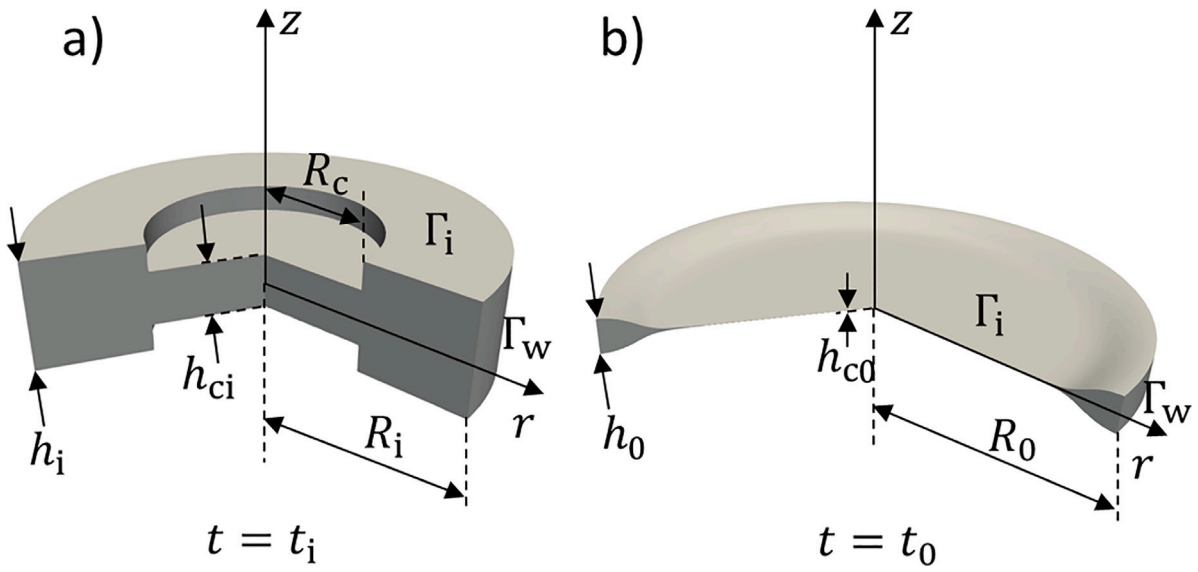

Fig. 1. (a) Geometry of an axisymmetric stepped film at the beginning of the stretching phase ($t = t_i$), having inner radius R_c, outer radius R_i, thickness at the center h_{ci} and at the edge h_i. The film is radially stretched at a constant strain rate $\dot{\epsilon}$. (b) Geometry of the film at the end of the stretching phase/beginning of the leveling phase ($t = t_0$), having outer radius R_0, thickness at the center h_{c0} and thickness at the edge h_0.

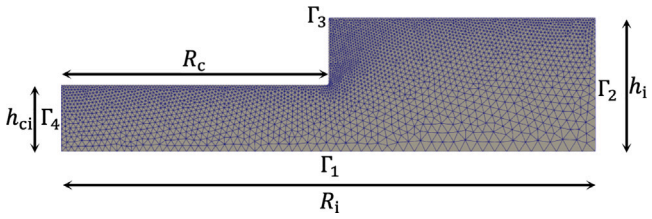

Fig. 2. Initial geometry and mesh of the axisymmetric 2D computational domain.

In this work, we present a numerical investigation based on FEM simulations aimed at elucidating the effects of viscoelasticity on the stretching and relaxation dynamics of freestanding films. Specifically, the analysis is divided into two stages: an initial film formation phase induced by biaxial extensional deformation, followed by a relaxation phase characterized by leveling flow. The influence of different stretching velocities and rheological models, i.e., Oldroyd-B (OB) and Giesekus (GSK) constitutive equations [21], on the behavior of the film is systematically investigated.

2. Problem outline

The initial geometry of the system considered in our study, shown in Fig. 1a, takes inspiration from the work by Ilton et al. [13] and consists of a stepped circular liquid film with inner radius R_c and outer radius R_i. The central, thinner region of the film has initial thickness h_{ci}, whereas the outer, thicker region has thickness h_i. During the first phase of the simulations, the film is radially stretched with constant strain rate $\dot{\epsilon}$ (see Eq. (8)) until it reaches a final outer radius R_0 (see Fig. 1b). At this point, it is allowed to relax under the combined action of surface tension, viscosity, and elasticity. The initial stepped geometry with sharp corners is almost instantaneously smoothed by surface tension, resulting in a sigmoidal film profile. Throughout this paper, the subscript 'i' identifies quantities evaluated at the beginning of the stretching phase, whereas the subscript '0' refers to the end of the stretching phase/beginning of the relaxation phase.

Owing to the geometry of the film, axial symmetry around the vertical axis, z, can be assumed. In addition, under the hypothesis of negligible gravitational effects, planar symmetry with respect to $z = 0$ can be also assumed. Hence, an axisymmetric two-dimensional computational domain is considered in the simulations, whose initial shape is reported in Fig. 2, along with the unstructured triangular computational discretization (mesh). Given isothermal, incompressible, and inertialess flow conditions, the film dynamics is governed by the continuity and momentum balance equations in the Stokes regime. To model the viscoelastic behavior of the film, both the Oldroyd-B (OB) and Giesekus (GSK) constitutive equations [21] are employed. In particular, the OB model describes viscoelastic fluids with constant shear viscosity, e.g., dilute polymer solutions, whereas the GSK model incorporates a nonlinear anisotropic drag term that allows prediction of shear thinning behavior and provides a more accurate description of polymer solution rheology.

In the formulation of the mathematical model, the following characteristic scales are introduced. The final outer radius of the film, R_0, is chosen as the characteristic length, whereas the inverse of the (constant) strain rate applied during the stretching phase, $1/\dot{\epsilon}$, is chosen as the characteristic time. Consequently, the characteristic velocity is $R_0\dot{\epsilon}$. Finally, the characteristic stress is $\eta_0\dot{\epsilon}$, where η_0 denotes the (zero-shear) viscosity of the fluid, corresponding to the sum of the 'solvent' and 'polymer' contributions, η_s and η_p. Based on such reference quantities, we can identify the expressions of the 'constitutive' dimensionless groups that characterize the dynamics of the system, namely, the Weissenberg number $\mathrm{Wi} = \lambda\dot{\epsilon}$ (λ being the relaxation time of the liquid), which is the ratio of fluid and the flow characteristic times, the capillary number $\mathrm{Ca} = \eta_0\dot{\epsilon}R_0/\gamma$ (γ being the surface tension between the liquid and the surrounding air), which is the ratio of viscous and surface forces acting on the film, here falling in the range $0.125 - 6.25$, and the viscosity ratio $\beta = \eta_s/\eta_0$, which is the ratio of the solvent to the (zero-shear) total viscosity of the liquid, equal to 0.4 in all the simulations whose results are presented in this paper. Additional 'geometric' dimensionless parameters are the ratio of center to edge initial thickness, h_{ci}/h_i, the ratio of center to outer initial radius R_c/R_i, and the ratio of final to initial outer radius R_0/R_i (see Fig. 1). In this paper, the values of those parameters are fixed to $h_{ci}/h_i = 0.8$ (except in Appendix), $R_c/R_i = 0.5$, and $R_0/R_i = 5$.

Given the aforementioned definitions, the mass and momentum balance equations on the film in the dimensionless form read

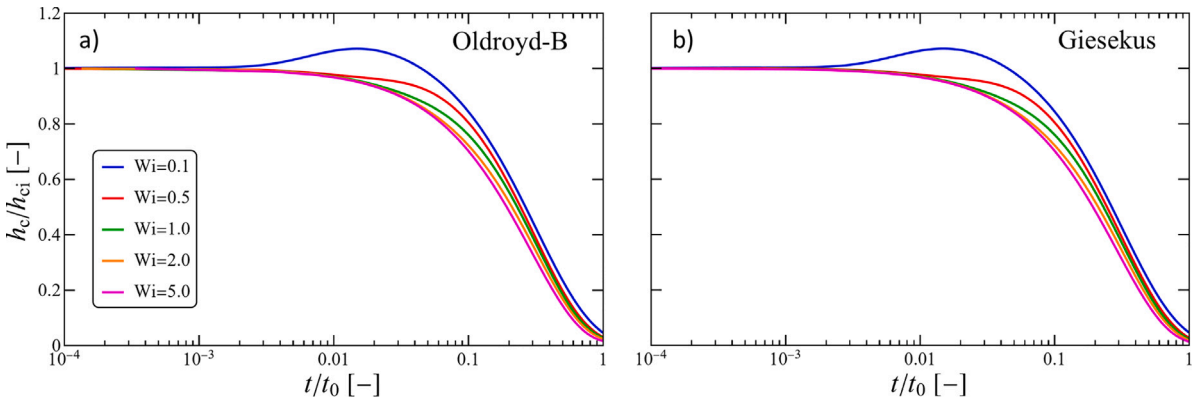

Fig. 3. Dynamics of the normalized thickness at the center of OB (a) and GSK (b) films during stretching at different values of Wi (see legend). Log scale is adopted on the horizontal axes.

$$\boldsymbol{\nabla}\cdot\boldsymbol{u}=0, \tag{1}$$

$$-\boldsymbol{\nabla}p+\beta\nabla^2\boldsymbol{u}+\boldsymbol{\nabla}\cdot\boldsymbol{\tau}=\boldsymbol{0}, \tag{2}$$

respectively, where $\boldsymbol{u}$ is the liquid velocity, p is the pressure, and $\boldsymbol{\tau}$ is the viscoelastic extra-stress tensor, for which the OB and GSK constitutive equations in the dimensionless form read

$$\mathrm{Wi}\overset{\nabla}{\boldsymbol{\tau}}+\boldsymbol{\tau}=2(1-\beta)\boldsymbol{D}, \tag{3}$$

$$\mathrm{Wi}\overset{\nabla}{\boldsymbol{\tau}}+\frac{\alpha\mathrm{Wi}}{1-\beta}\boldsymbol{\tau}^2+\boldsymbol{\tau}=2(1-\beta)\boldsymbol{D}, \tag{4}$$

where $\boldsymbol{D}=(\boldsymbol{\nabla u}+\boldsymbol{\nabla u}^{\mathrm{T}})/2$ is the rate-of-deformation tensor and α is the mobility parameter of the GSK model, modulating shear thinning and strain hardening, which is equal to 0.2 wherever the GSK fluid is considered in this work. It is straightforward to see that, when $\alpha=0$, the GSK constitutive equation degenerates into the OB one.

On Γ_1 and Γ_4 (see Fig. 2), the dimensionless boundary conditions are

$$\boldsymbol{u}\cdot\boldsymbol{n}=0,$$
$$(\boldsymbol{I}-\boldsymbol{nn})\cdot(\boldsymbol{T}\cdot\boldsymbol{n})=\boldsymbol{0}, \tag{5}$$

where $\boldsymbol{n}$ is the outwardly directed unit vector normal to the boundary, $\boldsymbol{I}$ is the identity tensor, and $\boldsymbol{T}$ is the total stress tensor in the fluid (the sum of the Newtonian and viscoelastic contributions). On the free surface Γ_3, the non-dimensional Young–Laplace condition is applied, reading

$$\mathrm{Ca}\boldsymbol{T}\cdot\boldsymbol{n}=-\boldsymbol{n}\cdot\boldsymbol{\nabla n}. \tag{6}$$

Finally, on Γ_2, the condition of zero tangential stress, i.e., axial slip,

$$(\boldsymbol{I}-\boldsymbol{nn})\cdot(\boldsymbol{T}\cdot\boldsymbol{n})=\boldsymbol{0} \tag{7}$$

holds true during both the stretching and the relaxation phases, whereas the normal velocity is

$$\boldsymbol{u}\cdot\boldsymbol{n}=\dot{\varepsilon}r \tag{8}$$

during the stretching phase and

$$\boldsymbol{u}\cdot\boldsymbol{n}=0 \tag{9}$$

during the relaxation phase.

As regards the initial conditions, we assume that, at $t=0$, the film is stress-free.

3. Numerical method

The equations presented in the previous section are solved through the finite element method (FEM) with an arbitrary Lagrangian Eulerian (ALE) formulation, where second-order interpolation is employed for velocity and first-order interpolation is employed for pressure and stress. The numerical code makes use of stabilization techniques widely described in the literature, such as streamline upwind Petrov–Galerkin (SUPG) and log-conformation. Such approach has been already used to study the retraction of thin viscoelastic films with a hole inside [22–24]. All the details on the finite-elemet algorithm employed to track the film surface are given in Villone et al. [25].

The 2D axisymmetric computational domain is discretized by means of an unstructured mesh made of triangular elements, as shown in Fig. 2. During the simulations, as the liquid film is stretched radially, the elements of the mesh progressively deform, thus, every time the mesh quality, in terms of the shape of the 'worst' element in the domain, goes below a threshold, a remeshing is performed and the solution is projected from the old mesh to the new one [26,27].

Before running simulations, convergence tests have been performed, i.e., mesh resolution and time step for the numerical solution of the equations presented above have been chosen such that invariance of the results upon further refinements is ensured. For the simulations presented in this paper, we have found that meshes with an initial number of triangles of about 5500 and time steps in the order of $5\times10^{-4}/\dot{\varepsilon}$ are adequate. Second-order time integration is used.

4. Results

Fig. 3 shows the dynamics of the thickness at the center of OB (a) and GSK (b) films, normalized to the initial value, during the stretching phase at different values of Wi, as reported in the legend. On the horizontal axes, the time is made dimensionless through division by the duration of the film stretching phase, t_0. For both fluids, and for Wi in between 0.5 and 5.0, the same qualitative behavior is observed, namely, a monotonic decrease of the thickness at the center of the film due to the applied biaxial extensional deformation. Specifically, for $t/t_0\gtrsim0.01$, the larger Wi the faster the thinning at film center. On the other hand, at Wi = 0.1, h_c/h_{ci} first increases until attaining a maximum, then it starts to decrease. This behavior is ascribed to the fact that, at such low Wi-value, the capillary leveling due to the 'stepped' profile of the film is initially more effective in making the thickness at the center increase by draining liquid from the peripheral zone, then, at longer time, biaxial stretching makes the film thickness decrease as in the cases at larger Wi. The results of additional simulations at two different values of h_{ci}/h_i are included in Appendix to further elucidate the influence of capillary leveling occurring during film stretching. It is also worth remarking that the values of the Weissenberg number considered in this paper are of the same order of magnitude as those experimentally attained in previous works dealing with similar problems, like, for example, the inflation of viscoelastic bubbles [23].

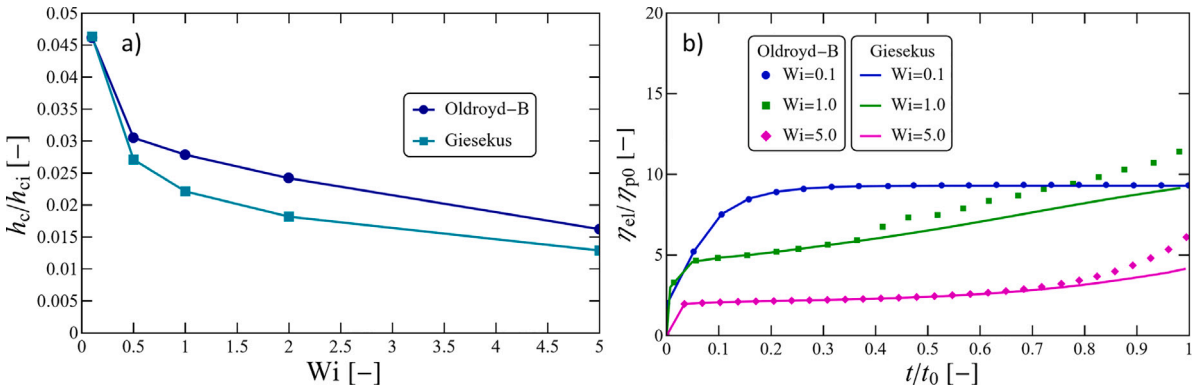

Fig. 4. (a) Normalized thickness at the center of the film at the end of the stretching phase as a function of Wi for OB (dark blue) and GSK (light blue) fluids. (b) Time evolution of the normalized extensional viscosity at the center of OB (symbols) and GSK (lines) films during stretching at different values of Wi (see legend).

Although the stretching dynamics of OB and GSK films appears qualitatively similar whatever Wi (see Fig. 3), the comparison of the thickness at the center of the film at the end of the stretching phase as a function of Wi shown in Fig. 4a reveals quantitative differences between the two fluids. Specifically, for all Wi-values except 0.1, the GSK film exhibits a lower final thickness compared to the OB one. This behavior can be attributed to the different rheological responses of the two fluids. Fig. 4b shows the time evolution of the normalized extensional viscosity at the center of OB and GSK films during stretching at Wi = 0.1, 1.0, and 5.0, as reported in the legend. The extensional viscosity at the film center is defined as $\eta_{el}(t) = |T_{rr}(t) - T_{zz}(t)|/\dot{\epsilon}_c(t)$, with $\dot{\epsilon}_c(t) = (-1/h_c(t))dh_c(t)/dt$, and it is normalized by the zero-shear polymer viscosity, η_{p0}. At Wi = 0.1, the extensional viscosity of both fluids monotonically increases to a plateau and the data corresponding to the two models perfectly overlap. This can be attributed to the fact that, at such low value of the Weissenberg number, the elastic effects are modest, making the difference between the two cases negligible. At larger Wi-values, however, significant deviations appear: in particular, in the second part of the film stretching phase, the OB model predicts an increasingly higher extensional viscosity than the GSK model. This discrepancy arises from the intrinsic differences between the constitutive equations. On the one hand, the OB model arises from the linear elastic dumbbell theory, which allows for unbounded polymer chain extension. As a result, the extensional viscosity diverges when Wi exceeds the critical value of 0.5. In contrast, the GSK model incorporates an anisotropic drag term, parameterized by α, which accounts for the constraints imposed to each polymer chain by the surrounding ones, thus limiting chain extensibility. Consequently, no divergence of the viscosity is predicted, as the latter tends to a high-Wi plateau value, whose magnitude is inversely proportional to α. When $\alpha = 0$, the GSK model degenerates into the OB model, recovering divergence Wi ≥ 0.5. Since we perform simulations where OB films are stretched at Wi-values above 0.5, it is important to clarify that the onset of viscosity divergence occurs on time scales longer than the stretching times considered here. Hence, as shown in Fig. 4b, the viscosity of OB films remains finite within the stretching time window at every Wi.

When inertial effects are negligible, the leveling dynamics of Newtonian films is exclusively governed by the interplay between surface tension and viscous dissipation. On the other hand, when viscoelastic fluids are considered, an additional contribution comes from the elastic energy stored by the material during the stretching phase, which can significantly affect the film relaxation behavior and must be considered in the analysis. The amount of elastic energy stored by a viscoelastic fluid strongly depends on its deformation history. A way of quantifying it is by computing the trace of the conformation tensor $\boldsymbol{c} = (\lambda/\eta_p)\boldsymbol{\tau} + \boldsymbol{I}$ [21].

Fig. 5 presents the maps of the trace of the conformation tensor, tr($\boldsymbol{c}$), in the film cross section at the end of the stretching phase for OB (a) and GSK (b) films at Wi = 0.1, 1.0 and 5.0 (from top to bottom). For both the fluids, the higher Wi the higher tr($\boldsymbol{c}$), especially at the center of the film, indicating larger elastic energy accumulation due to faster deformation (compared to the fluid relaxation time). At Wi = 0.1, tr($\boldsymbol{c}$) tends to tr($\boldsymbol{I}$) = 3 throughout the whole film cross section for both the OB and GSK constitutive equations. In other words, when the deformation is slow compared to the fluid relaxation time, the film relaxes the elastic stress during the stretching phase, thus there is no elastic energy accumulated at the end of the latter. At larger Wi-values (see second and third row in Fig. 5), a film made of OB fluid exhibits much more stored elastic energy than one made of GSK fluid. This might appear counterintuitive if one looks at the factor $1/\eta_p$ multiplying $\boldsymbol{\tau}$ in the definition of $\boldsymbol{c}$, as the extensional viscosity of OB films is larger than that of GSK films (see Fig. 4b), but the inspection of the viscoelastic stress maps at the end of the stretching phase reveals that OB films have a higher stress level than GSK films, which compensates for viscosity increase, thus resulting in a larger amount of stored elastic energy (tr($\boldsymbol{c}$)). As an illustrative example, Fig. 6 displays the maps of the normalized elastic normal stress difference, $|\tau_{rr} - \tau_{zz}|/(\eta_0\dot{\epsilon})$, in the film cross section at the end of the stretching phase for OB and GSK films at Wi = 5.0.

As discussed above, film stretching at different values of Wi yields different elastic energy storage in the material. This significantly affects the subsequent relaxation dynamics. Fig. 7 presents the evolution of the normalized thickness at the center of OB (a) and GSK (b) films during relaxation after stretching at different values of Wi, as reported in the legend. It is worth specifying that the film thickness is normalized by the value it will attain upon complete leveling, $h_{c\infty}$, namely, the height of a cylinder with a radius equal to that attained by the film at the end of the stretching phase, R_0, and containing the same fluid volume as the deformed film. Instead, the time is made dimensionless by subtracting the duration of the stretching phase, t_0, and dividing by the viscoelastic fluid relaxation time, λ.

For an OB fluid, the curves in Fig. 7a indicate that the larger Wi the 'further' the film central thickness starts from its asymptotic final value, i.e., the more the film has thinned in its central part during the stretching phase. On the other hand, the larger Wi the stronger the short-time thickness increase (except the case at Wi = 0.1, represented by the blue curve, where the normalized thickness already starts very close to 1 and almost does not change in the considered time window). This reflects the increasing amount of elastic energy stored at increasing Wi, resulting in a more prompt elastic recovery from the deformation imposed during the stretching phase. The elastic nature of such phenomenon is confirmed by the fact that it occurs over a time span of the same order of magnitude as the fluid relaxation time. Interestingly, after such time, all the curves at Wi from 0.5 to 5.0 reach the plateau value $h_c/h_{c\infty} \simeq 0.7$, indicating the end of elasticity-driven leveling. Of course, capillary forces will drive the film to the

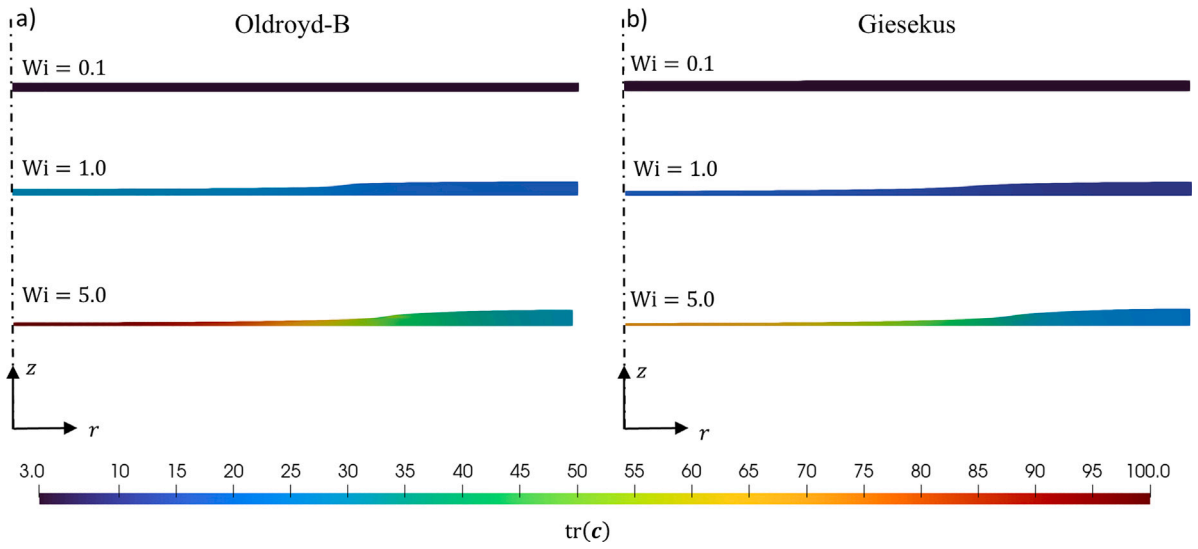

Fig. 5. Color maps of the trace of the conformation tensor, tr($\boldsymbol{c}$), in the film cross section at the end of the stretching phase for OB (a) and GSK (b) films at Wi = 0.1, 1.0 and 5.0 (from top to bottom).

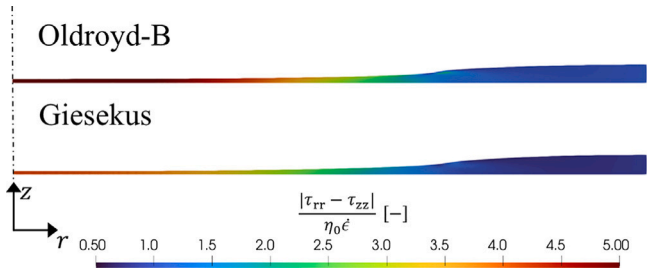

Fig. 6. Color maps of the normalized elastic normal stress difference, $|\tau_{rr}-\tau_{zz}|/(\eta_0\dot{\epsilon})$, in the film cross section at the end of the stretching phase for OB and GSK films at Wi = 5.0.

final equilibrium configuration having $h_c/h_{c\infty}=1$, but, given the time step ensuring the convergence of the simulations (equal to $5\times10^{-4}/\dot{\epsilon}$, as reported in Section 3), the computational time needed to see the film reach such configuration would have be unbearable (moreover, the investigation of capillary leveling is not the focus of this work). Instead, at Wi = 0.1, the stretching phase is so slow that no elastic energy is stored in the film at its end (see Fig. 5) and, consequently, the film does not exhibit any elastic recovery. In addition, the greatest part of capillary leveling occurs during the stretching phase itself, as indicated by the fact that, at $(t-t_0)/\lambda=0$, $h_c/h_{c\infty}$ is already very close to 1.

The curves in Fig. 7b indicate that, also for a GSK fluid, the larger Wi the 'further' the film central thickness starts from its asymptotic final value. However, the relaxation dynamics of GSK films exhibits relevant differences compared to that of OB ones, except the case at Wi = 0.1, where the very same behavior is observed. For Wi from 0.5 to 5.0, the film central thickness remains almost constant for about 0.1 time units (a slight increase is seen at Wi = 5.0), then it decreases until reaching a minimum and starting to increase again. Such thickness reduction becomes more pronounced as Wi increases. Therefore, unlike OB films, which undergo elastic leveling after the end of the stretching phase, GSK films display elastic 'anti-leveling'.

To assess whether this phenomenon is due to capillary forces, we estimate the capillary leveling characteristic time as $t_{lev,c}=\eta R_0^2/(\gamma\Delta h_0)$, where $\Delta h_0=h_0-h_{c0}$ is the difference between the thickness at the edge and at the center of the film at the end of the stretching phase. The evaluation of this quantity in the case characterized by the largest Δh_0-value, i.e., at Wi 5.0, yields $t_{lev,c}\simeq400\lambda$, indicating that capillary-driven leveling occurs on a time scale about two orders of magnitude larger than elastic effects, which are, then, responsible for anti-leveling.

Indeed, the latter stems from the evolution of the distribution of the elastic energy within the film during relaxation. The top row of Fig. 8 presents the contour plots of the conformation tensor trace for OB (a) and GSK (b) films during the first 3 time units of the relaxation phase after stretching at Wi = 5.0. On the vertical axis, the radial coordinate is normalized to the film radius at the end of the stretching phase, R_0. It is worth remarking that, in this representation, the film is pseudo-monodimensional, since, given r, tr($\boldsymbol{c}$) does not change in the axial direction. It is evident that the OB film retains a significantly higher amount of elastic energy in the central region (low r/R_0) during the initial part of relaxation ($t\lesssim0.1$). Furthermore, the elastic energy accumulated in the central part persists over a longer time compared to the GSK film, which dissipates it more rapidly. Therefore, the central region of the OB film has a strong elastic reaction to the deformation imposed during the stretching phase (which has made it thin), thus the thickness at the center of the film significantly increases during the first part of the relaxation phase. As a consequence, the central zone of the film drains fluid from the peripheral one, making the thickness at the film edge decrease (of course, thickness variations at large radial distance from the symmetry axis are much slighter that at the center due to mass conservation). The snapshots in Fig. 8c, taken at four time-values during the relaxation phase, show how the central thickness consistently increases, while the edge thickness slightly decreases, during elastic energy dissipation. In contrast, the central region of the GSK film has a little elastic reaction to the deformation imposed during the stretching phase, making the thickness at the center slightly increase during the earliest part of the relaxation phase, until attaining a maximum at $(t-t_0)/\lambda\simeq0.08$. Afterwards, the residual elastic energy accumulated at the center of the film is no longer sufficient to 'drive' the central thickness increase; on the contrary, since also the periphery of the film has been compressed during film stretching and contains residual elastic energy, the situation turns upside down, with the thickness at the film edge starting to increase due to elastic reaction, thus draining fluid from the film center, which causes a net decrease in central thickness, the hallmark of the aforementioned anti-leveling behavior. The snapshots in Fig. 8d further elucidate such scenario.

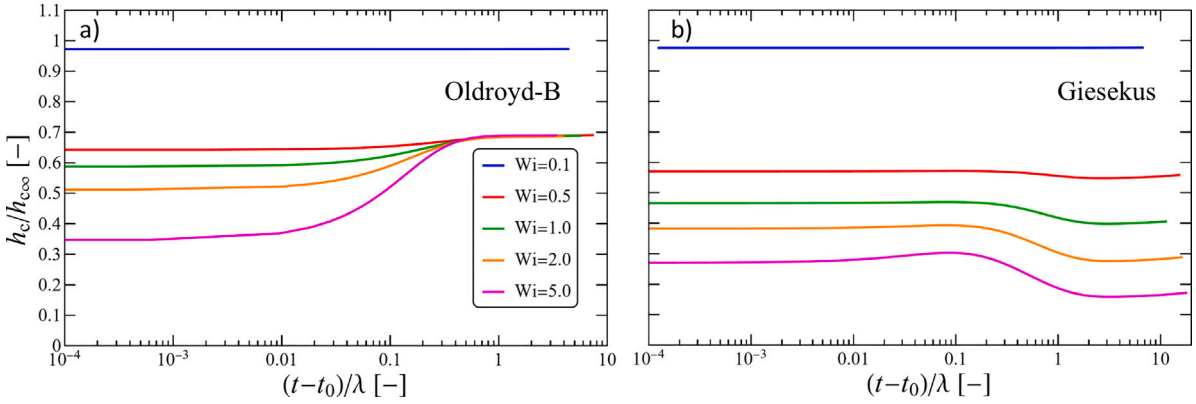

Fig. 7. Dynamics of the normalized thickness at the center of OB (a) and GSK (b) films during relaxation after stretching at different values of Wi (see legend). Log scale is adopted on the horizontal axes.

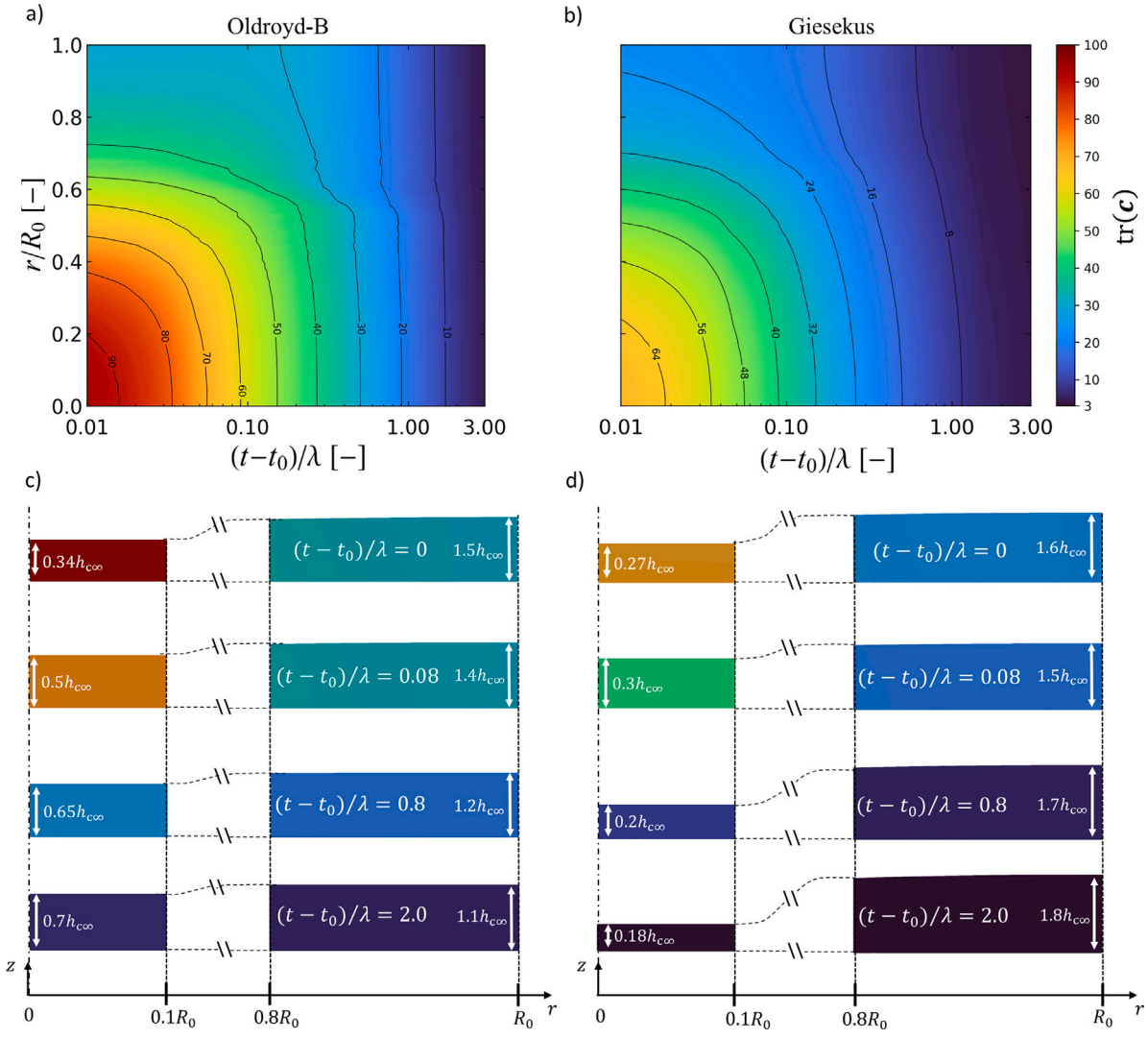

Fig. 8. Top row: contour plots of the conformation tensor trace, tr(c), along the normalized radial direction, r/R_0, for OB (a) and GSK (b) films during the first 3 time units of the relaxation phase after stretching at Wi = 5.0. Log scale is adopted on the horizontal axes. Bottom row: color maps of tr(c) in the central and peripheral parts of the film cross section for OB (c) and GSK (d) fluids at $(t-t_0)/\lambda$ = 0, 0.08, 0.8, and 2.0 during the relaxation phase.

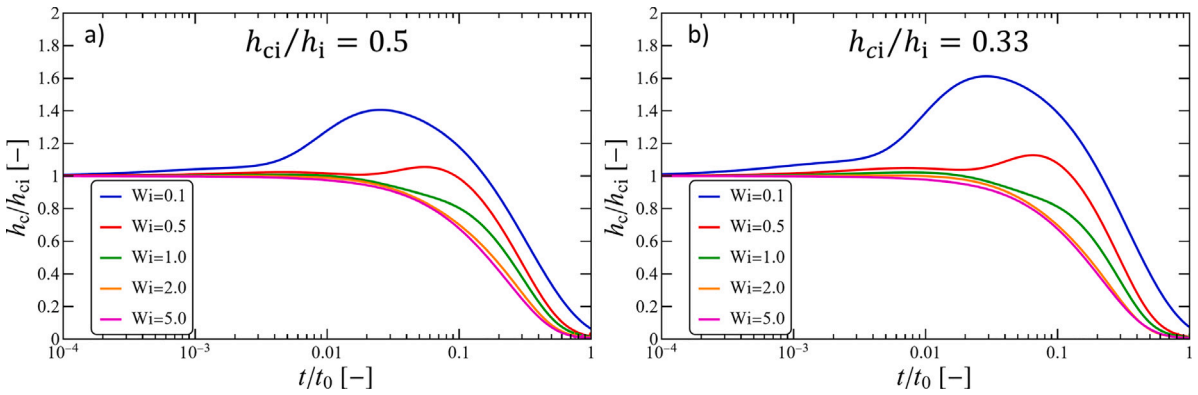

Fig. A.9. Dynamics of the normalized thickness at the center of OB films during stretching at different values of Wi (see legend) and $h_{ci}/h_i = 0.5$ (a) and 0.33 (b). Log scale is adopted on the horizontal axes.

5. Conclusions

In this study, we investigate the biaxial stretching and subsequent relaxation of circular viscoelastic freestanding liquid films using finite-element numerical simulations. We perform a parametric analysis by systematically varying the Weissenberg number (Wi) during the stretching phase to elucidate the relative contributions of elasticity, surface tension, and strain-dependent viscosity to the film dynamics. To characterize the fluid viscoelastic behavior, we employ two rheological models, namely, the Oldroyd-B (OB) and Giesekus (GSK) constitutive equations.

Starting from an axisymmetric stepped geometry, we observe that, at low Wi, film leveling occurs concurrently with stretching due to the dominance of capillary effects over elastic behavior. Conversely, at higher Wi, the film primarily undergoes thinning during the stretching phase, whereas leveling occurs during the relaxation phase. During the stretching stage, a similar evolution of the thickness at the center of the film is observed for OB and GSK constitutive equations. However, quantitative discrepancies arise, with the OB films showing larger thickness than GSK films at the end of the stretching phase. This can be attributed to the larger extensional viscosity experienced at the film center by the OB fluid, which resists film thinning more effectively than the GSK fluid.

Furthermore, we observe that, given the Wi-value characterizing the stretching phase, OB films store consistently more elastic energy than GSK films, quantified through the trace of the conformation tensor. This significantly influences the film relaxation dynamics. OB films show an increase in the central thickness, whose extent becomes more relevant at increasing Wi, indicating a strain recovery process driven by elasticity, referred to as 'elastic leveling'. On the contrary, GSK films display a reduction in central thickness, whose extent becomes more relevant at increasing Wi. We call this 'elastic anti-leveling'. Such contrasting behavior depends on the evolution of the spatial distribution of elastic energy within the film during relaxation. Indeed, in OB films, the central region retains a high level of elastic energy, promoting relaxation toward the undeformed state and draining fluid 'inward' from the peripheral region; on the other hand, in GSK films, the elastic energy in the central region is lower and the outer, thicker region dominates the elastic response, draining fluid from the central region and making it thin.

Our results highlight the critical role of viscoelasticity in governing the stretching and relaxation dynamics of freestanding liquid films, elucidating, in particular, the role of fluid rheology, which can determine even opposite effects in film relaxation dynamics.

CRediT authorship contribution statement

Davide Amoroso: Writing – original draft, Visualization, Validation, Software, Investigation, Formal analysis, Data curation, Conceptualization. **Massimiliano M. Villone:** Writing – review & editing, Visualization, Validation, Supervision, Software, Methodology, Investigation, Formal analysis, Data curation, Conceptualization.

Declaration of competing interest

The authors declare that they have no known competing financial interests or personal relationships that could have appeared to influence the work reported in this paper.

Acknowledgement

The authors thank M.A. Hulsen at the Eindhoven University of Technology (TU/e) for the access to the TFEM software libraries.

Appendix. Film stretching at different aspect ratio

Fig. A.9 illustrates how the normalized thickness at the center of an OB film evolves at different values of Wi, as reported in the legend, and of the height of the 'step' between the central and peripheral regions, namely, $h_{ci}/h_i = 0.5$ (panel a) and 0.33 (b). The curves suggest that increasing the initial height of the step enhances the capillary driving force, thus promoting more pronounced leveling during the film stretching phase [28]. Notably, unlike the case at $h_{ci}/h_i = 0.8$ shown in the main text, a surface-tension-driven temporary increase in film central thickness during film stretching is observed even at Wi = 0.5 when h_{ci}/h_i is decreased to 0.5 and 0.33. In particular, the lower h_{ci}/h_i the more relevant such phenomenon. Further results for films made of GSK fluid are not shown because the qualitative behavior does not differ significantly from that of the OB films under the same conditions.

Data availability

Data will be made available on request.

References

[1] P.-G. Gennes, F. Brochard-Wyart, D. Quéré, Capillarity and Wetting Phenomena, translation of the French ed., Springer, New York, NY, 2010.
[2] P. Tabeling, Introduction to Microfluidics, Repr., Oxford University Press, Oxford [u.a.], 2011.
[3] D.Y.C. Chan, E. Klaseboer, R. Manica, Film drainage and coalescence between deformable drops and bubbles, Soft Matter 7 (6) (2011) 2235–2264, http://dx.doi.org/10.1039/c0sm00812e.
[4] P. Iaccarino, Z. Wang, A. Marfuggi, S. Russo, V. Ferraro, G. Vitiello, S. Coppola, E. Di Maio, Thin free-standing liquid films manipulation: device design to turn on/off gravity in flow regimes for thickness map control and for material structuring, Soft Matter 21 (8) (2025) 1455–1470, http://dx.doi.org/10.1039/d4sm00951g.

[5] O.K.C. Tsui, Polymer thin films, in: Series in soft condensed matter, (v. 1) World Scientific Publishing Co Pte Ltd, Singapore, 2008, Description based on publisher supplied metadata and other sources..
[6] I.B. Ivanov, D.S. Dimitrov, Hydrodynamics of thin liquid films: Effect of surface viscosity on thinning and rupture of foam films, Colloid Polym. Sci. 252 (11) (1974) 982–990, http://dx.doi.org/10.1007/bf01566619.
[7] W. Cheng, M.J. Campolongo, S.J. Tan, D. Luo, Freestanding ultrathin nanomembranes via self-assembly, Nano Today 4 (6) (2009) 482–493, http://dx.doi.org/10.1016/j.nantod.2009.10.005.
[8] A. Silberberg, Distribution of conformations and chain ends near the surface of a melt of linear flexible macromolecules, J. Colloid Interface Sci. 90 (1) (1982) 86–91, http://dx.doi.org/10.1016/0021-9797(82)90400-3.
[9] P.D. Howell, H.A. Stone, On the absence of marginal pinching in thin free films, European J. Appl. Math. 16 (05) (2005) 569, http://dx.doi.org/10.1017/s095679250500625x.
[10] J. Teichroeb, J. Forrest, Direct imaging of nanoparticle embedding to probe viscoelasticity of polymer surfaces, Phys. Rev. Lett. 91 (1) (2003) 016104, http://dx.doi.org/10.1103/physrevlett.91.016104.
[11] Z. Fakhraai, J.A. Forrest, Measuring the surface dynamics of glassy polymers, Science 319 (5863) (2008) 600–604, http://dx.doi.org/10.1126/science.1151205.
[12] O. Bäumchen, R. Fetzer, K. Jacobs, Reduced interfacial entanglement density affects the boundary conditions of polymer flow, Phys. Rev. Lett. 103 (24) (2009) 247801, http://dx.doi.org/10.1103/physrevlett.103.247801.
[13] M. Ilton, M.M.P. Couchman, C. Gerbelot, M. Benzaquen, P.D. Fowler, H.A. Stone, E. Raphaël, K. Dalnoki-Veress, T. Salez, Capillary leveling of freestanding liquid nanofilms, Phys. Rev. Lett. 117 (16) (2016) 167801, http://dx.doi.org/10.1103/physrevlett.117.167801.
[14] A. Oron, S.H. Davis, S.G. Bankoff, Long-scale evolution of thin liquid films, Rev. Modern Phys. 69 (3) (1997) 931–980, http://dx.doi.org/10.1103/revmodphys.69.931.
[15] A. Münch, B.A. Wagner, T.P. Witelski, Lubrication models with small to large slip lengths, J. Engrg. Math. 53 (3–4) (2005) 359–383, http://dx.doi.org/10.1007/s10665-005-9020-3.
[16] J.D. McGraw, N.M. Jago, K. Dalnoki-Veress, Capillary levelling as a probe of thin film polymer rheology, Soft Matter 7 (17) (2011) 7832, http://dx.doi.org/10.1039/c1sm05261f.
[17] J.D. McGraw, T. Salez, O. Bäumchen, E. Raphaël, K. Dalnoki-Veress, Self-similarity and energy dissipation in stepped polymer films, Phys. Rev. Lett. 109 (12) (2012) 128303, http://dx.doi.org/10.1103/physrevlett.109.128303.
[18] V. Ferraro, M.M. Villone, V. Tkachenko, L. Miccio, L. Lombardi, D. Tammaro, E. Di Maio, G. D'Avino, P.L. Maffettone, Axisymmetric bare freestanding films of highly viscous liquids: Preparation and real-time investigation of capillary leveling, J. Colloid Interface Sci. 596 (2021) 493–499, http://dx.doi.org/10.1016/j.jcis.2021.03.102.
[19] S. Sekhar, V. Shankar, Instability of ultrathin viscoelastic freestanding films, Phys. Fluids 33 (3) (2021) http://dx.doi.org/10.1063/5.0042409.
[20] S. Sekhar, A. Sharma, V. Shankar, Instability and rupture of ultrathin freestanding viscoelastic solid films, Phys. Rev. E 106 (2) (2022) 024803, http://dx.doi.org/10.1103/physreve.106.024803.
[21] R.G. Larson, Constitutive equations for polymer melts and solutions, in: Butterworths Series in Chemical Engineering, Butterworths, Boston, 1988, Includes bibliographical references and indexes.
[22] M.M. Villone, G. D'Avino, E. Di Maio, M.A. Hulsen, P.L. Maffettone, Modeling and simulation of viscoelastic film retraction, J. Non-Newton. Fluid Mech. 249 (2017) 26–35, http://dx.doi.org/10.1016/j.jnnfm.2017.09.005.
[23] D. Tammaro, R. Pasquino, M.M. Villone, G. D'Avino, V. Ferraro, E. Di Maio, A. Langella, N. Grizzuti, P.L. Maffettone, Elasticity in bubble rupture, Langmuir 34 (19) (2018) 5646–5654, http://dx.doi.org/10.1021/acs.langmuir.8b00520.
[24] M.M. Villone, M.A. Hulsen, P.L. Maffettone, Numerical simulations of viscoelastic film stretching and retraction, J. Non-Newton. Fluid Mech. 266 (2019) 118–126.
[25] M. Villone, M. Hulsen, P. Anderson, P. Maffettone, Simulations of deformable systems in fluids under shear flow using an arbitrary Lagrangian Eulerian technique, Comput. Fluids 90 (2014) 88–100.
[26] H.H. Hu, N.A. Patankar, M.Y. Zhu, Direct numerical simulations of fluid–solid systems using the arbitrary Lagrangian–Eulerian technique, J. Comput. Phys. 169 (2) (2001) 427–462.
[27] N.O. Jaensson, M.A. Hulsen, P.D. Anderson, Stokes–Cahn–Hilliard formulations and simulations of two-phase flows with suspended rigid particles, Comput. & Fluids 111 (2015) 1–17.
[28] L.E. Rodd, T.P. Scott, J.J. Cooper-White, G.H. McKinley, Capillary break-up rheometry of low-viscosity elastic fluids, Appl. Rheol. 15 (1) (2005) 12–27, http://dx.doi.org/10.1515/arh-2005-0001.